Time-Resolved Small-Angle Neutron Scattering Study of Polyethylene Crystallization from Solution

HOWARD WANG

Department of Materials Science and Engineering, Michigan Technological University, Houghton, Michigan 49931

Received 20 October 2003; revised 29 January 2004; accepted 9 February 2004
DOI: 10.1002/polb.20181
Published online in Wiley InterScience (www.interscience.wiley.com).

ABSTRACT: With time-resolved small-angle neutron scattering (TR-SANS), the crystallization kinetics of polyethylene from deuterated *o*-xylene solutions upon a temperature jump have been investigated. On the basis of a morphological model of coexisting lamellar stacks and coil chains in solution, experimental data have been quantitatively analyzed to provide structural information, such as the lamellar long period, the lamellar crystal thickness, the thickness of the amorphous layers between lamellae, the degree of crystallinity, and the crystal growth rate at various degrees of undercooling. The viability of TR-SANS for studying polymer crystallization is demonstrated through the consistency of these measurements and well-established knowledge of polyethylene crystallization from xylene solutions. One unique feature of this experimentation is that both the growth of lamellar crystals and the condensation of coil chains from solution are monitored simultaneously. The ratio of the crystal growth to the chain consumption rate decreases rapidly with a decreasing degree of undercooling. The Avrami analysis suggests that the growth mechanism approaches two-dimensional behavior at higher temperatures, and this is consistent with the observation of an increasing ratio of the sharp-surface area to the bulk crystal growth rate with temperature. The limitations, possible remedies, and potentials of TR-SANS for studying polymer crystallization are discussed. © 2004 Wiley Periodicals, Inc. J Polym Sci Part B: Polym Phys 42: 3133–3147, 2004
Keywords: crystallization; polyethylene (PE); neutron scattering

INTRODUCTION

Crystallization of long-chain molecules has been extensively studied over the last half-century and is reasonably well understood;[1–6] nevertheless, some fundamental issues are still under investigation and debate. Those include the experimental determination of the equilibrium melting temperature of polymers,[7–10] the metastability of polymer crystals,[11,12] and the mechanism of homogeneous nucleation.[13–21] Those general issues in polymer crystallization also appear in the subfield of solution crystallization. The equilibrium dissolution temperatures (T_d^0's) of polyethylene (PE) in xylene have been carefully measured,[22–24] and several theories have been developed to predict T_d^0.[25–28] However, inconsistencies between experimental results and theoretical predictions remain, as pointed out in previous[24] and recent publications.[29] On the other hand, the growth kinetics depend on the crystal habits and crystallographic directions;[30,31] a general mean field description of crystallization kinetics could be difficult.[13]

As it becomes clear that a further understanding of polymer crystallization lies in the quanti-

Correspondence to: H. Wang (E-mail: wangh@mtu.edu)
Journal of Polymer Science: Part B: Polymer Physics, Vol. 42, 3133–3147 (2004)

tative characterization of molecular dynamics during nucleation and growth, computer simulations at the molecular level could play an important role. Recent chain dynamic simulations have captured essential features of long-chain crystallization.[32–35] On the experimental side, the requirement for probing individual chains in real time points to the need for *in situ* scattering and spectroscopic methods.

Since theoretical development by Ruland[36] and Strobl and Schneider,[37] small-angle X-ray scattering (SAXS) with synchrotron X-ray radiation has been successfully applied to probing primarily the lamellar-level structural evolution in real time and has played an important role in recent debates on how early-stage density fluctuations lead to melt crystallization.[14–17] Complementing X-ray scattering, small-angle neutron scattering (SANS) has also been widely used in determining material structures, particularly multicomponent soft-matter systems. The advantage of SANS is the convenience of isotope labeling for enhancing or reducing the contrast between components and, therefore, highlighting or concealing certain components for structural determination. SANS plays an important role in determining the structure and dynamics of polymeric systems, which possess increasingly greater complexity. A good example demonstrating the powerfulness of SANS was documented by Richter et al.,[38] who investigated the hierarchical ordering of crystalline–amorphous block copolymers (BCPs) in solutions.

SANS has been applied to determining the fundamentals of polymer crystallization since the early development of the technique. For example, Wignall et al.[39] revealed chain clustering upon crystallization; Keller and others[40–42] illustrated the nature of chain folding at the basal plane of lamellar crystals; and Beaucage and Stein[43] gave deep insights into thermodynamics and chain conformations in polymer blends that exhibit both phase separation and crystallization.

Because of the considerably smaller flux of neutron sources in comparison with that of synchrotron X-ray radiation, applications of SANS to kinetic studies have been limited. There are only a handful of reports on using time-resolved small-angle neutron scattering (TR-SANS) to probe structural evolution. Most TR-SANS studies are on surfactant or lipid systems;[44–52] other topics include protein folding kinetics,[53] spin glasses,[54] colloidal particle aggregation kinetics,[55] phase-separation kinetics of short alkane mixtures,[56] and template-assisted mineralization.[57] In polymer research, TR-SANS has been used to study the kinetics of spinodal decomposition[58–62] and early-stage nucleation and growth[63,64] in phase-separating polymer blends, the relaxation of composition fluctuations in polymer mixtures after a pressure jump,[65,66] the relaxation upon plastic deformation,[67] unimer exchange kinetics in BCP micelles,[68] BCP-templated mineralization,[69] BCP micellization,[70] and so forth.

Applications of TR-SANS to studying polymer crystallization are yet to be explored. We hope that the use of this technique will bring new insights into a broad perspective of the old field of polymer crystallization. In this article, we demonstrate the use of TR-SANS for studying the kinetics of polymer crystallization from solution. A model system of PE fractions in xylene is used. By analyzing the kinetic data with a morphological model, we quantify essential structural parameters, such as the lamellar long period, the lamellar crystal thickness, the thickness of amorphous layers between lamellae, the degree of crystallinity, and the crystal growth rate. The implications of the experimental findings are discussed.

THEORETICAL BACKGROUND

Early morphological studies have shown that PE crystals grown from not-so-dilute solutions (as in this report) can take various habits, such as pyramids, rotating terraces, lozenges, and dendrites, depending on the polymer concentration, the degree of undercooling (ΔT), the molecular weight, and so forth.[4–6] Those crystal habits are at length scales of micrometers to tens of micrometers, whereas multilayered crystals (lamellar stacks) dominate the features at tens to hundreds of nanometers.[4–6] The latter overlap with the aforementioned SANS scattering wavevector (Q) range and are the length scales of interest in this study. Accordingly, we consider a morphological model, as depicted in Figure 1(a), to describe the morphology evolution during polymer crystallization from solution. There are four components in the system: lamellar crystals and amorphous layers in lamellar stacks, coil chains in the solution, and the solvent. The differences in their neutron scattering length densities (SLDs) give the contrast for SANS. The SLD of the ith component (ρ_i) is defined as follows:

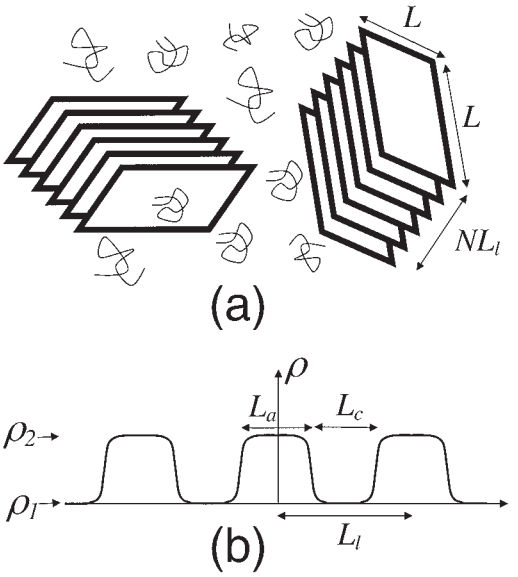

Figure 1. (a) Schematic illustration of the polymer morphology during isothermal crystallization. Polymers form lamellar stacks that coexist with random coils in the solvent. It is assumed that all lamellar stacks have $L \times L$ square lateral facets and N lamellar sheets separated by an average distance L_l. (b) Cross-sectional profile of lamellar stacks with L_l, L_c, and L_a. The SLDs of the crystals and amorphous layers are ρ_1 and ρ_2, respectively.

$$\rho_i = \frac{\sum b_j}{v_i} \tag{1}$$

where the summation is over the scattering length (b_j) of all atoms in the unit of volume v_i of that component. In this study, we define subscript i as the solvent (0), crystal (1), amorphous phase in lamellar stacks (2), and coils in solution (3). Under the incompressibility limit, the SLD of each component is constant. In this model, the structure of swollen chains in amorphous regimes of lamellar stacks is not considered. Rather, a homogeneous density is assumed. Several geometrical and structural parameters are denoted as follows: lamellar stacks are approximated by squares with lateral dimension L, and the number of slabs in a stack is N (both are assumed to be constant for all stacks); the long period (spacing) for average slab separations is L_l; and the average crystal and amorphous layer thicknesses are L_c and L_a, respectively. A cross-section profile of lamellar stacks is shown in Figure 1(b). Other parameters include the total volume fraction of polymer chains in the solution (ϕ_0), the volume fraction of crystals (ϕ_{cry} or ϕ_1), the volume fraction of amorphous layers (ϕ_2), the volume fraction of coils during crystallization (ϕ_{coil} or ϕ_3), the volume fraction of lamellar stacks (Φ_s), the average volume of individual lamellar stacks (V_s), and the volume of an individual chain (V_3).

With the solvent SLD (ρ_0) as a reference, the SLD difference for the ith component ($\Delta\rho_i$) is

$$\Delta\rho_i = \rho_i - \rho_0 \tag{2}$$

For a four-component system, a general expression of the total coherent scattering cross section per unit of volume is

$$\frac{d\Sigma}{d\Omega}(Q) = \sum_{i=1}^{3} \Delta\rho_i^2 S_{ii} + 2\sum_{i<j}^{3} \Delta\rho_i \Delta\rho_j S_{ij} \tag{3}$$

where Q is defined as

$$|Q| = \frac{4\pi}{\lambda} \sin\frac{\theta}{2} \tag{4}$$

where λ is the wavelength of the incident neutron and θ is the scattering angle. The partial scattering function is defined as

$$S_{ij}(Q) = \frac{1}{V}\int_V\int_{V'} \langle \Phi_i(r) \cdot \Phi_j(r') \rangle e^{iQ(r-r')} dr dr' \tag{5}$$

where the angle brackets denote the orientation average. The integration is performed over the entire sample volume (V), and $\Phi_i(r)$ describes the local volume fraction of the ith component at position r. If we assume that there is no third component in the lamellar stacks, $\Phi_1(r) + \Phi_2(r)$ is equal to 1; the relationships between the partial structure factors involving the two components are as follows:

$$S_{11} = S_{22} = -S_{12} \tag{6}$$

If we further assume no correlations between coils and lamellar stacks, S_{13} and S_{23} are both equal to 0. Thus, eq 3 could be simplified to

$$\frac{d\Sigma}{d\Omega}(Q) = (\Delta\rho_1 - \Delta\rho_2)^2 S_{11} + \Delta\rho_3^2 S_{33} \tag{7}$$

With this approach, the scattering due to the overall size of the lamellar stacks is neglected because in this study the length scales of typical stacks exceed the low-Q limit. Nevertheless, the contribution from the sharp interface is accounted for by the inclusion of a term following the Porod law, A_p/Q^β, in the total scattering cross section in eq 7. The Porod exponent (β) is 4 for ideal sharp surfaces and between 3 and 4 for surface fractals. The Porod coefficient (A_p) is proportional to the area of sharp surfaces.

The partial structure factors S_{11} and S_{33} can be calculated explicitly with the model depicted in Figure 1. With details of the calculation omitted, S_{11} can be expressed as follows:

$$S_{11}(Q) = \frac{\Phi_s}{V_s} \cdot S(Q) \cdot |F(Q)|^2 \tag{8}$$

where $S(Q)$ is the structure factor of lamellar stacking and $|F(Q)|^2$ is related to the form factor of individual lamellar slabs. The latter takes the form

$$|F(Q)|^2 = \frac{(\pi L)^2}{Q^2}\left[\frac{L_c \sin(QL_c/2)}{QL_c/2}\right]^2 \exp(-Q^2\sigma_{L_c}^2), \tag{9}$$

where the exponential term is due to the Gaussian distribution of the lamellar thickness with a spreading width constant (σ_{L_c}), according to the approach of Richter et al.[38] The structure factor has a compact form for an infinite number of lamellae in a stack:[38]

$$S(Q) = \frac{\sinh(Q^2\sigma_{L_l}^2/4)}{\cosh(Q^2\sigma_{L_l}^2/4) - \cos(QL_l)} \tag{10}$$

where σ_{L_l} is the Gaussian distribution width for the long period. For a finite number of N lamellae in a stack, the structure factor is[38]

$$S(Q) = 1 + \frac{2}{N}\sum_{n=1}^{N}(N-n)\cos(QL_l)\exp(-Q^2\sigma_{L_l}^2 n/4) \tag{11}$$

which can be used to describe the early stage of lamellar growth.

The scattering function of coils in the solution fits into a general formalism developed by Beaucage and Schaefer,[71] which smoothly joins the power-law behavior at high Q and the Guinier regime at low Q:

$$S_{33}(Q) = G\exp(-Q^2R_g^2/3) + B\left[erf\left(\frac{wQR_g}{\sqrt{6}}\right)\right]^{3\alpha} Q^{-\alpha} \tag{12}$$

where R_g is the radius of gyration of the polymer coil, $w = 1.06$ is a constant, and $Q^{-\alpha}$ is the asymptotic power law at high Q. The prefactors G and B are

$$G = \Phi_3(1-\Phi_3)V_3 \text{ and } B = \frac{G\alpha}{R_g^\alpha \Gamma(\alpha)} \tag{13}$$

where $\Gamma(\alpha)$ is the gamma function. Through the combination of eqs 7–13, the scattering cross section of a polymer solution during crystallization can be quantitatively analyzed.

Table 1. Material Parameters Used for Fitting the SANS Spectra

	Density (g/cm^3)	Coherent SLD ($\times 10^{-6}$ Å^{-2})	Incoherent Cross Section (cm^{-1})
Coil	0.87	−3.11	6.0
Crystal	1.00	−3.57	6.89
Solvent	0.952	5.87	0.11[a]

[a] This value was obtained from the best fit of the solution scattering data. The incoherence background of *o*-xylene with 99 atom % deuterium and 1 atom % hydrogen was 0.14 cm^{-1}, indicating a higher deuteration level than that at 99 atom %, which was the lower boundary of the manufacture specifications.

EXPERIMENTAL

The PE in this study was a standard reference material (SRM 1483) from the National Institute of Standards and Technology (NIST) and had a weight-average molecular weight of 32,100 g/mol and a polydispersity of 1.11. The equilibrium melting temperature was 144.8 °C, and T_d^0 in xylene was about 110 °C.[22–24,29,30] V_3 was 55,175 Å^3. The solvent was nearly fully deuterated *o*-xylene (>99 atom % deuterium) purchased from C/D/N Isotopes, Inc. A PE solution with $\phi_0 = 0.0034$ was used in this study. The material parameters used for fitting the SANS spectra are listed in Table 1.

The scattering parameters for the amorphous layer in the lamellar stack, the third component of the system, were not readily available. The consequence of this uncertainty is discussed.

TR-SANS measurements were performed with the 8-m SANS instrument at the NIST Center for Neutron Research. Incident neutrons of $\lambda = 10$ Å and a sample-to-detector distance of 3.84 m yielded a range of scattering wavevectors (0.006 $Å^{-1} < Q < 0.1$ $Å^{-1}$). The neutron wavelength dispersion ($\Delta\lambda/\lambda = 0.15$) was mainly responsible for the resolution of the SANS measurements. In temperature jump experiments, the sample cell remained in a heating stage. The solution was first equilibrated at 120 °C for 10 min, cooled to 85 °C and kept there for 30 min, and further cooled to isothermal temperatures (T_{iso}'s), which ranged from 78.0 to 82.0 °C. SANS measurements started when the last setting-stage-temperature command was executed. The scattered neutrons were counted with a two-dimensional (2D) detector. After correction for background and detector efficiency and conversion to an absolute scale with the direct beam intensity, the 2D intensity was circularly averaged to yield the total scattering cross section of the sample, which included the incoherent scattering (a white background not shown in eq 7).

Separate measurements showed no significant structure developing during 30 min at 85 °C; this was also demonstrated in the time-dependent data, as shown later. The purpose of isothermal storage at an intermediate temperature was to reduce the temperature overshoot and the temperature equilibration time.

Because of the lack of active cooling units in the current setup, cooling was achieved by heat dissipation via convection. The equilibration of the stage temperature was monitored. Because the thermal mass of the heating stage was much larger than the solution in the sample cell, it was assumed that the sample temperature followed that of the stage. Figure 2 shows the evolution of the sample stage temperature upon a software-controlled temperature jump from 85.0 °C to various T_{iso}'s. The stage temperature reached equilibrium at 82.0 ± 0.2 °C after about 300 s, 81.0 ± 0.1 and 80.0 ± 0.1 °C after about 400 s, and 79 ± 0.2 and 78.0 ± 0.1 °C after about 500 s. The temperature overshot by about 1 °C at $T_{iso} = 82.0$ °C and by more than 2 °C at $T_{iso} = 78.0$ °C. Significant structure development occurred because of the temperature overshoot for $T_{iso} = 78.0$ °C, whereas structural changes during the temperature equilibration period were negligible for other higher T_{iso}'s. In the following, we analyze the crystallization kinetics at $T_{iso} > 78.0$ °C, whereas the final structure at 78.0 °C, which is presumably not sensitive to the initial thermal history, is also discussed.

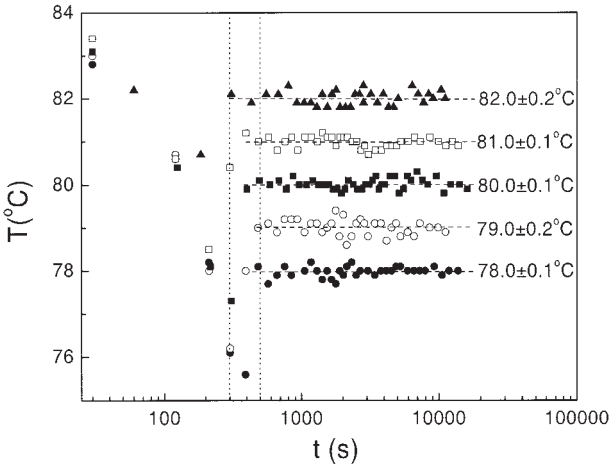

Figure 2. Variation of the stage temperature after a controller command that sets the stage from an initial temperature at 85 °C to various T_{iso}'s. The stage reaches temperature equilibrium after about 300 s at 82.0 ± 0.2 °C and after about 500 s at 78.0 ± 0.1 °C, as indicated by the vertical, dotted lines.

The time intervals for the data acquisition varied from 30 s during the initial stage to 20 min during the final stage of the isothermal crystallization. The time label for each SANS spectrum in an isothermal series was set to the ending time of the data acquisition.

RESULTS AND DISCUSSION

The SANS data were analyzed with eqs 7–13. For polymer solutions at high temperatures, eqs 12 and 13 were used. For the fitting of the TR-SANS spectra, the fitting parameters were taking random walks in the parameter space. Up to two variables were allowed to vary simultaneously. The time sequences of the SANS spectra were fitted with both chronicle and counter-chronicle orders, with the best parameters from the fitting of each spectrum being used as the input for fitting the next spectrum. The quality of fitting was controlled through the minimization of the conventional root-mean square of the χ parameter, which is defined as the difference between the experimental and theoretical values divided by

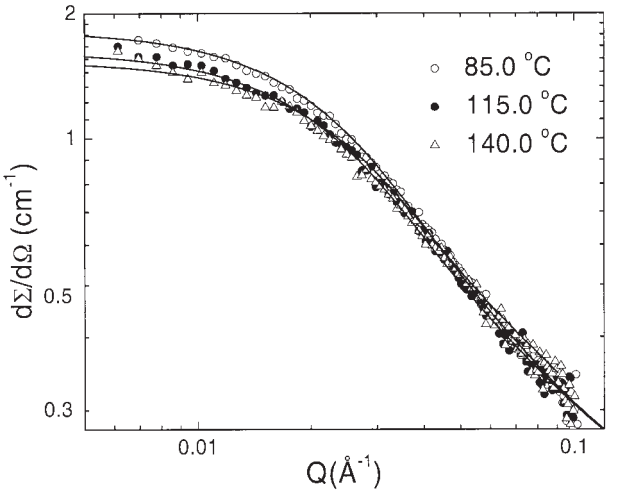

Figure 3. Scattering cross sections per unit of volume of polymer solutions at 85.0, 115.0, and 140.0 °C. The solid curves through the symbols are the best fits according to eqs 12 and 13. The apparent R_g value of the polymer coils is about 60 Å.

the statistical error. A typical value for the best fit was about 1 for the high-temperature solution or early-stage isothermal data and about 6 for late-stage isothermal spectra. The primary causes of this difference were the statistics of the data and the exactness of the model. The counting statistics of the solution data were poorer, whereas the model describing the coil chains was more accurate; on the contrary, the statistics were better for the late-stage crystallization data, whereas the morphological model was somewhat simplified.

Polymer Solution

The structure of PE solutions at elevated temperatures is discussed first. Figure 3 shows the scattering cross section of polymer solutions at 85.0, 115.0, and 140.0 °C. The solid curves through the symbols are the best fits. There is little variation of the scattering cross section as the temperature varies from 140.0 to 85.0 °C, and this is somewhat expected. The slight decrease in the scattering intensity with increasing temperature is mainly due to the change in the contrast factor, which becomes smaller at higher temperatures because of the thermal expansion. The slight upturn of the low-Q intensity at 140.0 °C may be due to the reduction in the solvent quality for PE as the boiling temperature of the solvent is approached.

The fits in Figure 3 give a power exponent of $\alpha = 1.65$ at high Q. Flory predicted that in a good solvent polymer chains take a fractal dimension of $d = 1/\nu$, with $\nu = 3/5$ the Flory exponent.[72] Scattering from such random coil solutions shows asymptotic power-law behavior (Q^{-d}). The SANS results from high-temperature solutions are consistent with this prediction. A chain dimension quantity could also be obtained from the fit ($R_g = 60$ Å).

In analyzing the TR-SANS data for crystallization kinetics, we assume that polymer chains in the solution are in the same random coil form, with the same R_g value and chain fractal dimension. With such assumptions, contributions to the neutron scattering intensity from the solution depend solely on the volume fraction of random coils and so can be easily separated from the scattering of lamellar crystal stacks.

Time-Dependent Spectra

Typical TR-SANS spectra are shown in Figure 4 after various times of isothermal storage at $T_{iso} = 81.0$ °C; the symbols represent the experimental data, and the curves are the best fits according to eqs 7–13. When the sample reaches temperature equilibrium after about 400 s, the scattering intensity is identical to that of the high-temperature solution within error. After a longer time at 81.0 °C, the scattering intensity increases dramatically. At the low-Q end, the increase is more than two orders of magnitude, from 2 to about 300 cm^{-1}. This change is due to the crystallization of

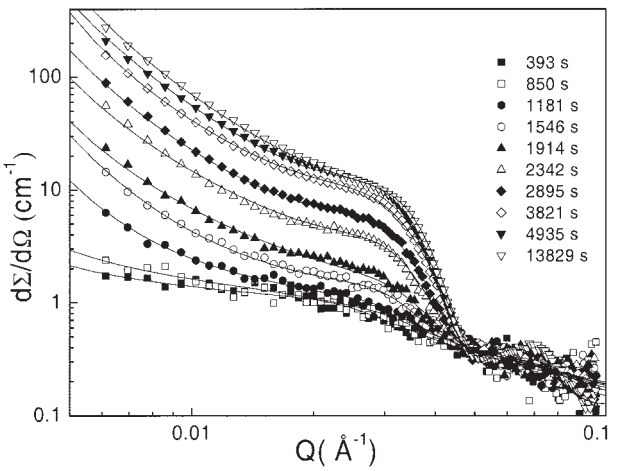

Figure 4. Time sequence of SANS spectra of PE solutions at $T_{iso} = 81.0$ °C. The symbols represent the experimental data, and the curves through the symbols are the best fits to the data. The low-Q intensity increases by more than two orders of magnitude.

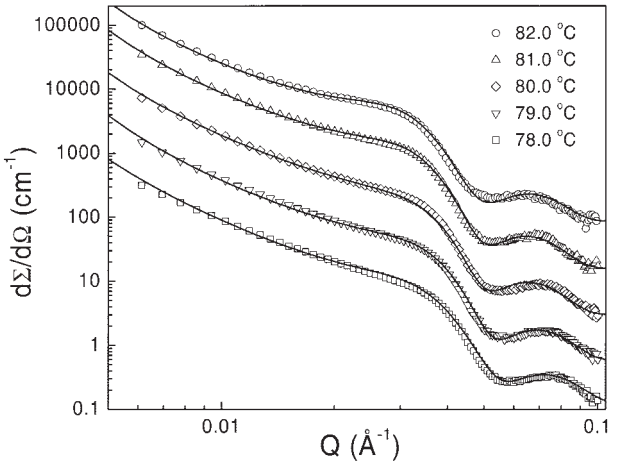

Figure 5. SANS spectra of PE solutions during the final stage of isothermal storage at 78.0, 79.0, 80.0, 81.0, and 82 °C. For clarity, higher temperature spectra are vertically offset by a factor of 5 with respect to lower temperature ones. The solid curves through the symbols are the best fits. The characteristic features of the spectra shift consistently to lower Q values with increasing T_{iso} values, suggesting larger feature dimensions at higher temperatures.

PE chains. The kinetics of crystallization are discussed in detail in the following sections.

The quality of model fitting is more clearly displayed in Figure 5, which shows the final spectra at various T_{iso}'s; the symbols represent the experimental data, and the curves through the data are the best fits. For clarity, the spectra at $T_{iso} > 78.0$ °C are vertically offset by a factor of 5 with respect to the adjacent ones. It is evident that the morphology model and the evaluation method for the corresponding scattering cross section are capable of capturing the essential features. A quick comparison of those spectra indicates that the characteristic features at $Q > 0.03$ Å^{-1} shift consistently toward lower Q as T_{iso} increases, and this suggests larger feature dimensions at higher temperatures. In the following sections, the feature dimensions and other quantities are analyzed from the fitting of the TR-SANS data, and their evolutions are discussed to illustrate the kinetics of polymer crystallization from solution.

Lamellar Structures

Quantifying the evolution of the lamellar structure is of primary importance in understanding the crystal growth. Figure 6 shows the time dependence of L_l, L_c, and L_a for crystals grown at $T_{iso} = 81.0$ °C. The lamellar parameters at $t < 2500$ s are not displayed because the structure is not fully developed. From about 4000 s to 7500 s, L_l decreases by about 10 Å. As L_c remains relatively constant, the change is mostly accommodated by the change in L_a. There are two possibilities that could result in such observations. One is that lamellar stacks relax to achieve better packing after their formation; the other is that lamellar stacks grown at a later time have better packing efficiency because they grow epitaxially from previously ordered lamellar stacks. Whether one mechanism is more plausible than the other depends on the time regime of the structural change; a comparison with the evolution of crystallinity is necessary. Figure 10 (shown later) shows that at 81.0 °C the time period of 4000–7500 s happens to cover the late-stage growth to the beginning of a plateau, so both mechanisms may play a role.

The final length parameters of lamellar stacks at various T_{iso}'s are shown in Figure 7. Both the final long period ($L_{l,f}$) and the final lamellar thickness ($L_{c,f}$) increase with T_{iso}. The final amorphous layer thickness ($L_{a,f}$) shows little variation with the temperature. Theoretically, L_c is related to $\Delta T = T_d^0 - T_{iso}$ through the relation $L_c = \delta L_c + 2\sigma_e T_d^0 / \Delta h_f \Delta T$, where σ_e is the surface energy of the folding plane, Δh_f is the heat of fusion at the equilibrium melting temperature, and δL_c is a constant predicted in kinetic theories to be 5–15 Å.[2] The inset of Figure 7 shows $1/(L_c - \delta L_c)$ as a function

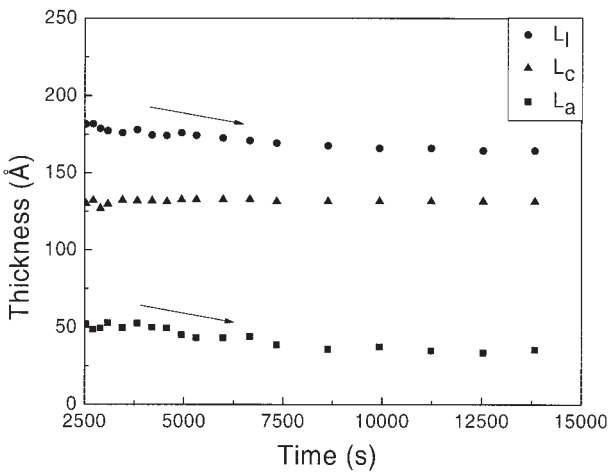

Figure 6. Evolution of L_l, L_c, and L_a at $T_{iso} = 81.0$ °C. From about 4000 to 7500 s, both L_l and L_a decrease by about 10 Å, as indicated by the arrows, whereas L_c remains relatively constant.

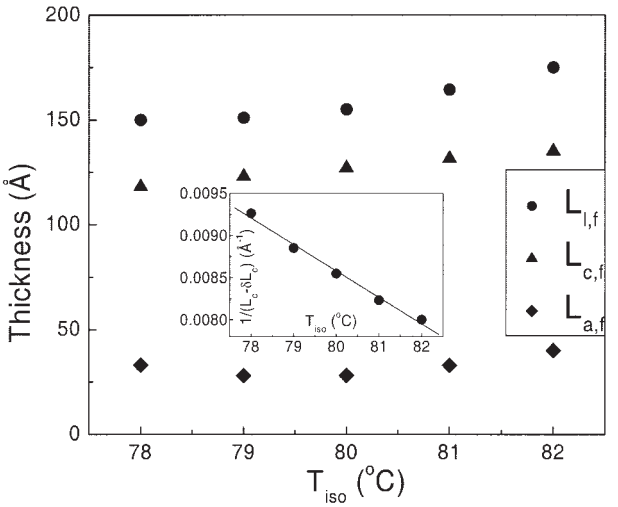

Figure 7. Final thickness parameters of lamellar stacks at various T_{iso}'s. Both $L_{l,f}$ and $L_{c,f}$ increase with T_{iso}. $L_{a,f}$ shows little variation with the temperature. The inset shows the inverse of $L_{c,f} - \delta L_c$ as a function of T_{iso}. Linear extrapolation to infinite crystal thickness gives an T_d^0 value of 107 ± 7 °C.

of T_{iso}, with δL_c assumed to be 10 Å. Linear extrapolation to zero gives $T_d^0 = 107 \pm 7$ °C, which is consistent with the literature value within error.[22–24,29,30] The values of L_c in this study are larger than those in a previous report for the same polymer (NIST SRM-1483) in xylene,[29] presumably because of several differences between the two experiments: (1) the solvent (hydrogenated *p*-xylene in ref. 29 vs deuterated *o*-xylene in this study), (2) the concentration (0.05 mass % in ref. 29 vs 0.34 vol %, or 0.31 mass %, in this study), (3) the thermal history (self-seeding in ref. 29 vs step cooling in this study), and (4) the measurements (*ex situ* measurements on filtered and dried crystals in ref. 29 vs *in situ* measurements in this study). Further investigations are necessary to identify the exact cause.

σ_{L_l} and σ_{L_c} are shown in Figure 8. Both σ_{L_l} and σ_{L_c} are relatively constant, with values around 70 and 7 Å, respectively. The apparent anticorrelation relationships between σ_{L_l} and σ_{L_c} implies that to a degree these two wobbling factors cannot be isolated from each other.

Degree of Crystallinity

The Q-independent coefficient of the partial scattering function $[S_{11}(Q)]$ is proportional to the product of Φ_s and the volume fraction of lamellar crystals in stacks and, therefore, proportional to ϕ_{cry}. The product of this coefficient and the contrast factor between the crystal and amorphous layers is obtained from model fitting. However, because the amount of *o*-xylene in the amorphous layers and, therefore, the contrast between the crystalline and amorphous layers in lamellar stacks are not known *a priori*, the degree of crystallinity cannot be calculated directly. To get around this difficulty, we estimate ϕ_{cry} from the evolution of the coil concentration in solution by assuming that the number of free coils condensed out of the solution equals the number of coils forming lamellar stacks. For this purpose, the variation of ϕ_{coil} is discussed first.

Figure 9 shows the evolution of ϕ_{coil} at various T_{iso}'s in semilogarithmic scales. The coil-to-crystal conversion takes place over an increasingly longer time period with the temperature. The final leveling-off values apparently also increase with temperature, as one would expect, when the driving force toward crystallization becomes smaller. However, at the final stage, the contribution of coil scattering to the total intensity is small; those values could just be reflecting the threshold values when the fitting becomes insensitive to the coil contribution. The inset shows the time for converting 50% PE from free coils to aggregates ($t_{0.5}$). This $t_{0.5}$ is different from the conventional half-time for crystallization. The solid curve in the inset is a guide. The magnitude of the rate of conversion (G_{coil}) is estimated from the linear region of the concentration variation, which is discussed later.

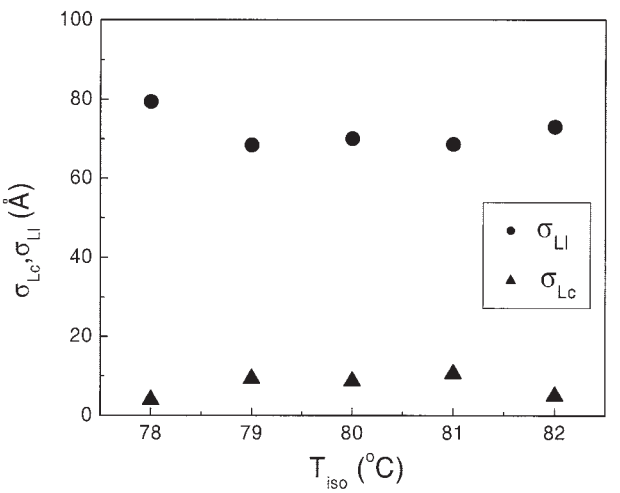

Figure 8. σ_{L_l} and σ_{L_c} at various temperatures. Both σ_{L_l} and σ_{L_c} are relatively constant, with values of approximately 70 and 7 Å, respectively.

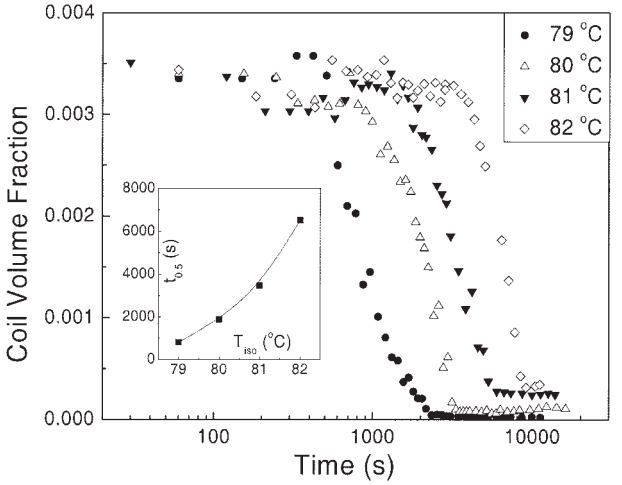

Figure 9. Evolution of the volume fraction of polymer chains in solution at 79.0, 80.0, 81.0, and 82 °C in semilogarithmic scales. The conversion from coils to crystals takes place over an increasingly longer time period with temperature. The inset shows the time for converting half of the chains from random coils in solution into crystal aggregates ($t_{0.5}$). This $t_{0.5}$ is different from the conventional half-time of crystallization. The solid curve in the inset is a guide.

We assume that at $t_{0.5}$, coils that have disappeared from the solution are all converted into lamellar stacks. The lamellar crystal stack parameters from the fit, as shown in Figure 6, indicate that the amorphous fraction (L_a/L_l) is a relatively constant quantity, about 0.20. If we assume that the coil chains and the solvent each occupy half the volume of the amorphous region, the fraction of the amorphous polymer is about 0.1. That value falls in the typical range of amorphous fractions, which is 10–25%.[4] Therefore, the volume fraction of crystals at $t_{0.5}$ is

$$\phi_{cry}(t_{0.5}) = \frac{d_a}{d_c}\left[1 - \frac{L_a}{2L_l}\right]^* \phi_{coil}(t_{0.5}) \qquad (14)$$

where d_a and d_c are the mass densities of the amorphous and crystalline PE, respectively. This crystallinity is proportional to the product of the contrast factor and the coefficient of $S_{11}(Q)$ at $t_{0.5}$, which is obtained from fitting. Applying this proportionality relationship to the entire crystallization process, with other constants being absorbed in the scaling factor, we can calculate $\phi_{cry}(t)$.

Figure 10 shows the evolution of ϕ_{cry} at various T_{iso}'s. The general features of polymer crystallization are qualitatively followed. Crystals grow more slowly at high temperatures, and the degree of crystallinity is higher at lower temperatures. The overall values are reasonable, except for those at 82.0 °C, which seem to be too high. The unique feature here is the simultaneous detection of scattering signals from both coil chains and lamellar crystals, which is not typically achievable in SAXS measurements. In this study, the sensitivity to the volume fraction of crystallinity is about 10^{-5}, being comparable to that of light scattering and exceeding that of SAXS.[17] The linear growth regions are fitted with lines whose slopes represent the crystallization rate (G_{cry}), which is discussed later. Although qualitatively satisfactory, rigorous quantification in this approach suffers from two facts: (1) the assumption that all chains precipitated from solution form lamellar stacks may not be valid at high temperatures and (2) the volume fraction of the solvent in amorphous regions is only a guess.

Alternatively, the degree of crystallinity can be estimated from the scattering invariant (Q_{inv}). In this approach, scattering signals from the incoherent background, free coils in solution, and sharp interfaces (Porod scattering) are subtracted from the measured intensity. Therefore, the experimentally determined scattering invariant for lamellar stacks per unit of volume of solution can be expressed as follows:

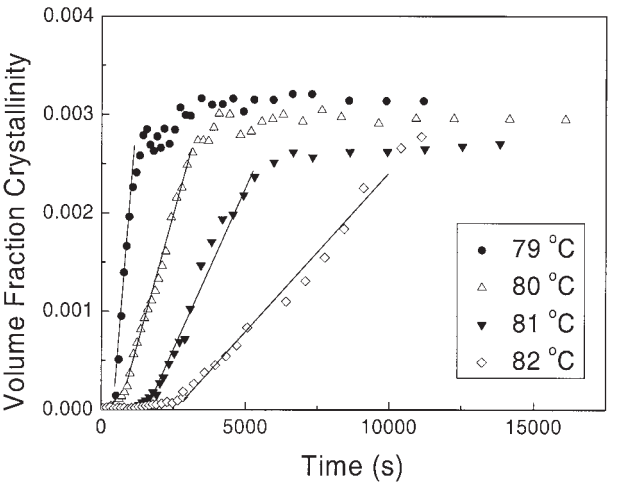

Figure 10. Evolution of the apparent volume fraction of crystallinity in solutions at various crystallization temperatures. Generally, crystals grow faster and the crystallinity levels off at a higher value at a lower T_{iso}. Linear growth regions have been fitted with lines, the slope of which quantifies the crystallization rate.

$$Q_{\text{inv}} = \frac{1}{2\pi^2}\int \frac{d\Sigma}{d\Omega}\Big|_{\text{lam}} Q^2 dQ = \frac{1}{2\pi^2}\int (\Delta\rho_1 - \Delta\rho_2)^2 S_{11} Q^2 dQ \quad (15)$$

where the integral is taken over the entire Q range. On the other hand, by definition, the scattering invariant is the mean-square SLD fluctuations or the magnitude of the correlation function at its origin. In a three-component system, because the coil contribution has been subtracted in the evaluation of Q_{inv} with eq 15,

$$Q_{\text{inv}} = \Delta\rho_1^2\phi_1 + \Delta\rho_2^2\phi_2 - (\Delta\rho_1\phi_1 + \Delta\rho_2\phi_2)^2 \quad (16)$$

where volume fractions of crystal and amorphous layers are related to the volume fraction of lamellar stacks through

$$\phi_1 = \Phi_s L_c/L_1 \text{ and } \phi_2 = \Phi_s L_a/L_1 \quad (17)$$

Therefore, in principle, with an experimentally determined Q_{inv} value and the coefficient for the lamellar partial structure factor, the two unknowns, Φ_s and $\Delta\rho_2$, can be solved exactly with eqs 8, 16, and 17. In practice, however, because of the limited Q range of the measurements and other complications such as coil structures within the amorphous region, this strategy can hardly be quantitative. In this study, the Porod scattering at low Q cannot be subtracted reliably because of the limited Q range for evaluation. This approach is more applicable to two-component systems such as a highly concentrated crystallizable polymer in a solvent, in which all solvent molecules reside in amorphous layers of lamellar stacks or, from another viewpoint, semicrystalline polymers with amorphous regions swollen by solvents.

Further SANS experiments could be helpful in solving these puzzles. With ultra-SANS, it is possible that during the early stage of structure development, the Guinier region for lamellar stacks can be resolved so that both the number density and average dimensions of lamellar stacks are directly measured. On the other hand, the contrast between the crystalline and amorphous region can be tuned by the crystallization of a polymer in a mixture of hydrogenated and deuterated solvents. With a few measurements at different compositions of isotope–solvent mixtures, the amorphous fraction in lamellar stacks can be determined. Those are topics for future investigations.

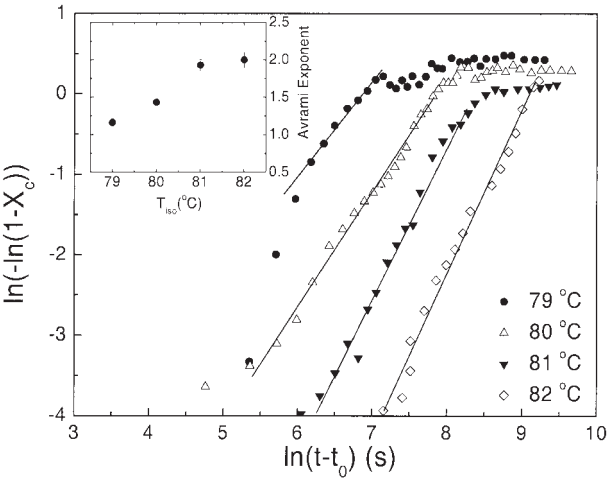

Figure 11. Avrami plot for PE crystallizing from solution at four temperatures. The slope from the linear fit reveals the Avrami exponents, which are shown in the inset. The Avrami exponents indicate that the crystallization mechanism may be 1D growth at lower temperatures and 2D growth at higher temperatures.

Crystallization Kinetics

ϕ_{cry} can be converted into a mass ratio crystallinity (X_c) of the total crystallizable polymers through $X_c = (d_c/d_a)(\phi_{\text{cry}}/\phi_0)$, which can be analyzed with the Avrami equation:

$$X_c = 1 - e^{-k(t-t_0)^n} \quad (18)$$

where k is the crystallization rate constant, n is the Avrami exponent, and t_0 is the induction time. Figure 11 shows the Avrami fit of the crystallization kinetic data. Here the induction time is an empirical quantity that gives a best representation of the Avrami law, that is, a large linear region in a plot of $\ln[-\ln(1 - X_c)]$ versus $\ln(t - t_0)$. In reality, crystallization starts before the t_0 value used for Figure 11. For example, signals can be reliably detected around 400 and 500 s at 80.0 and 81.0 °C, respectively, whereas t_0 has been chosen to be 500 and 1000 s at the corresponding temperatures. It has been previously argued that the dormant time for polymer crystallization depends on the measurement sensitivity.[17] A linear fitting of the data in Figure 11 reveals the Avrami exponents, which are shown in the inset. The Avrami exponents vary from about 1.2 at 79.0 °C

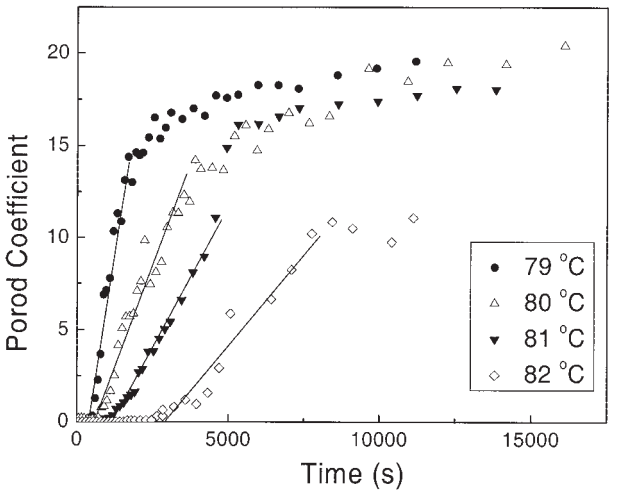

Figure 12. Evolution of A_p (in an arbitrary unit scale) at various T_{iso}'s. Linear growth regions have been fitted with lines, the slopes of which quantify the growth rate of the area of the sharp lamellar basal planes.

to about 2 at 82.0 °C. This increase suggests a change from a high tendency of branching-out [one-dimensional (1D)] growth at low T_{iso}'s to lateral (2D) growth at high T_{iso}'s.

Figure 12 shows the evolution of A_p at various T_{iso}'s. A_p follows the general feature of crystallinity, as in Figure 10. Linear growth regions of A_p's are fitted with lines, the slopes of which quantify the growth rate of the area of sharp lamellar basal planes (G_{sur}). The β values that result from the best fits are 3.58, 3.7, 3.7, and 4.0 for T_{iso} of 79.0, 80.0, 81.0, and 82.0 °C, respectively, suggesting sharper interfaces of lamellar stacks at higher T_{iso}'s. Because the power exponents are different, caution should be taken in direct comparison of A_p's.

Figure 13 compares various linear rates during isothermal crystallization. They are G_{cry}, G_{sur}, and G_{coil}. The G_{sur} values are multiplied by a constant (i.e., shifted vertically in a logarithmic scale) to be shown in the same plot. The logarithms of these rate quantities decrease with increasing temperature. The inset shows the ratio of the surface to the volume crystallinity growth rate (G_{sur}/G_{cry}), which increases with temperature, and the ratio of the crystal growth rate to the free coil reduction rate (G_{cry}/G_{coil}), which decreases with temperature. The × and + symbols in the inset are discussed later.

The G_{sur}/G_{cry} ratios indicate that the amount of the sharp surface produced per unit of volume of growing crystals increases with temperature, suggesting better faceted crystals grown at higher temperatures. The reduction of the G_{cry}/G_{coil} ratio with temperature implies that the portion of coils that condense from solution while not participating in making ordered lamellar crystals increases with regard to the total amount of condensed chains. At T_{iso} = 79.0 °C, the ratio is 0.9, which is close to a complete transformation within error. On the other hand, at 82.0 °C, the ratio drops to close to 0.5, pointing to the validity of the assumption of the complete transformation from consumed coils to lamellar stacks for calculating the crystallinity in Figure 10. The crystallinity at 82.0 °C in Figure 10 is, therefore, overestimated.

To avoid the problem, we use another method to evaluate the crystallinity. Because the assumption of complete conversion from condensed coils to lamellar stacks seems to be valid at 79.0 C, with an apparent 10% error, the crystallinity values at other temperatures are normalized by the crystallinity/intensity ratio at the final stage of 79.0 °C. Figure 14 shows the evolution of the thus obtained volume fraction of crystallinity. The crystallinity values at 82.0 °C are now more reasonable; however, another anomaly is found at lower T_{iso}'s, at which the final crystallinity at 81.0 °C becomes higher than that at 80.0 °C and comparable to that at 79.0 °C. A possible problem with a single crystallinity/intensity scale for different temperatures is that crystal perfection is

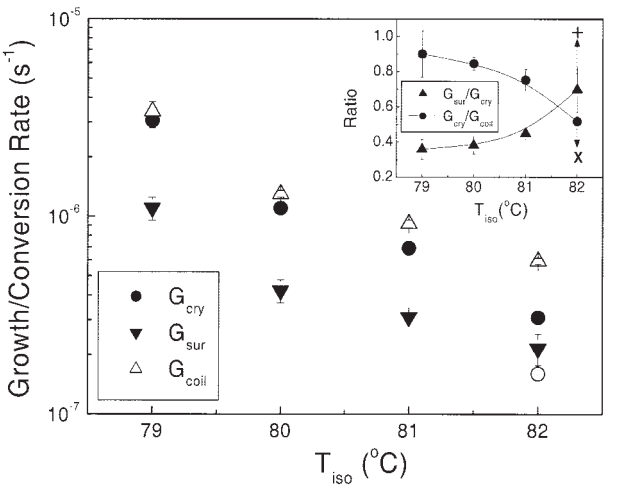

Figure 13. G_{cry}, G_{sur}, and G_{coil}. G_{sur} has been shifted vertically to be shown in the same plot. The inset shows G_{sur}/G_{cry}, which increases with temperature, and G_{cry}/G_{coil}, which decreases with temperature (the open circle in the main graph and the × and + symbols in the inset are discussed in the text).

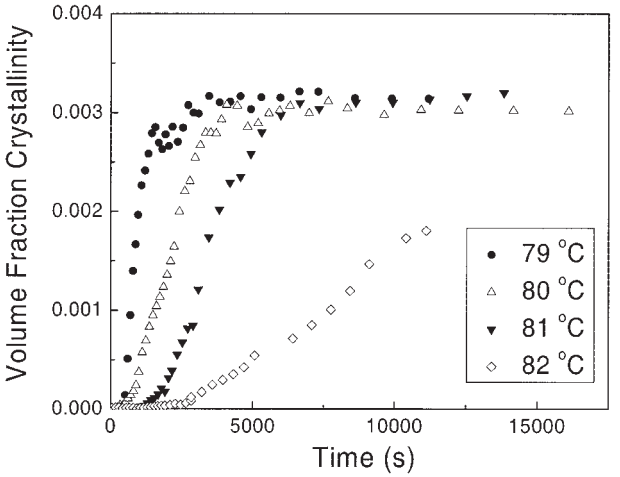

Figure 14. Evolution of the volume fraction degree of crystallinity in solutions at various crystallization temperatures normalized by the crystallinity/intensity ratio at 79 °C. This treatment gives reasonable crystallinity values at 82.0 °C. However, an anomaly is shown at lower T_{iso}'s, at which the final crystallinity at 81.0 °C becomes higher than that at 80.0 °C and comparable to that at 79.0 °C.

different at different temperatures; better ordering perfection leads to a higher scattering intensity, which is incorrectly translated into a higher degree of crystallinity.

Figure 14 resembles most features in Figure 12 for A_p. A close comparison of those two at $T_{iso} < 82.0$ °C reveals that at long times, ϕ_{cry} levels off, whereas A_p continues to grow; this suggests reorganization toward better surface perfection. The new crystal growth rates are obtained from Figure 14. The only significant modification is at 82.0 °C, which is shown in Figure 13 as an open circle. Accordingly, the ratios in the inset of Figure 13 find new values at 82.0 °C. As indicated by the arrows, the solid circle is shifted to the $\times$ sign, and the triangle is shifted to the + sign. Therefore, the temperature effect on those ratios becomes more pronounced. That confirms the assertions that the formation of lamellar crystals lags behind the condensation of the chains from solution and that crystals grow better faceted surfaces at higher temperatures. The corresponding change of the Avrami exponent at 82 °C is small, from 2 to about 1.8, which is within the error of those quantities. Therefore, the previous statement on growth dimensionality still holds.

Those comparisons seem to give a picture that is qualitatively consistent with what we know about polymer crystallization from solution: at low temperatures and large undercoolings, crystallization kinetics are fast, crystals may form fibril structures with rough interfaces, and the degree of crystallinity is high; at high temperatures and small undercoolings, crystallization kinetics are slow, crystals form 2D flat structures with sharp interfaces, and the crystallinity is low. More rigorous SANS measurements with a large Q range and various contrasts could be used to provide a more quantitative assessment of the degree of crystallinity, but direct methods such as thermal analysis and X-ray diffraction are more accurate and convenient for determining the crystallinity.

SANS versus SAXS

SANS is an important technique complementing SAXS for materials studies. Particularly for the study of soft matter, which is dominated by light elements and in many cases lacks good structural order, neutron scattering plays an important role. The similarities and differences in their applications to polymers have been described in details in a monograph.[73] The applications of neutron scattering to studying polymer crystallization, for which X-ray scattering and diffraction are very powerful, are relatively few. Here we discuss one particular feature of SANS for studying polymer crystallization, that is, the source of contrast coming from the composition heterogeneity rather than the density heterogeneity.

SANS detects the heterogeneity of neutron SLD in samples, whereas X-ray scattering detects the electron density differences. This makes SANS of little use for studying crystallization in homopolymers. However, in a complex system with multiple components, contrast variation and contrast matching could be very powerful for isolating scatterings from different components and solving the structure. In this study, SANS is capable of distinguishing both coil chains and lamellar crystals in solution and, therefore, provides more information than SAXS for determining the evolution kinetics: it not only sees new structures forming, but it also measures the consumption of raw materials for making these new structures.

The large contrast induced by deuterium labeling to a degree compensates the small flux of the currently available neutron sources. This is particularly true when the density differences be-

tween the features are small, for example, during the early-stage structure development due to fluctuations in melts and during polymer aggregation before crystallization in solutions. In that sense, SANS possesses the advantages of both SAXS and light scattering, namely, suitable length scales and high sensitivity. Another issue is thermally excited density fluctuations, which are usually neglected in the formulation of the scattering profile under the assumption of incompressibility. However, in soft matter, this may not always be a safe assumption. X-ray scattering is certainly more susceptible to density fluctuations than neutron scattering because the contrast for the latter comes primarily from the compositional differences, which may not be affected significantly by density fluctuations. Therefore, in the study of soft matter, SANS spectra may appear cleaner than SAXS spectra for weak scattering objects.

Neither the resolution nor the flux of the current SANS instrument can compete with synchrotron X-ray radiation, and this limits SANS as a viable tool for studying fast kinetics and highly ordered structures. This situation is expected to change to a degree when the new spallation neutron source at the Oak Ridge National Laboratory becomes available in a few years. With a brighter neutron source and time-of-flight detection to simultaneously cover a reasonable Q range, it is hoped that the development of early-stage structures can be resolved.

CONCLUSIONS

Using a model system of well-characterized PE fractions in *o*-xylene, we have demonstrated the feasibility of using TR-SANS for studying polymer crystallization from solution. On the basis of a morphological model of coexisting lamellar stacks and coil chains in solution, all the essential quantities have been characterized. The quantifications provide a physical picture that is consistent with well-established knowledge of PE crystallization from xylene solutions. Uniquely in this measurement, both the rate of the crystal growth and that of the free coil condensation are monitored simultaneously. The detection sensitivity to the volume fraction of crystallinity is as low as 10^{-5}, which is comparable to that of light scattering.

We stress that the compositional origin of the contrast in TR-SANS makes the technique useful in understanding early-stage structures of polymer crystallization in blends and in solutions. As a great portion of the knowledge of polymer crystallization is obtained through density contrast between the crystalline and amorphous phases (e.g., optical microscopy, electron microscopy, and X-ray scattering), it would be beneficial to probe polymer crystallization with the contrast associated with compositional differences.

There are several difficulties limiting the full utility of TR-SANS for studying polymer crystallization. Two obvious obstacles are the inability to know the SLD of the solvent-swollen amorphous regions in lamellar stacks and the limited Q range at both low Q (Porod law regime) and high Q (coil scattering). Another concern is the dependence on models for understanding the scattering data. Although model fitting could accommodate more complexities than the correlation function approach, it is still rather limited to well-defined and simple structures. In this study, the structural model is well-established, and this results in plausible data evaluations, whereas on some other occasions, structures may not be known *a priori*. In view of these difficulties, it is important for SANS measurements to be complemented by other methods, such as morphological techniques, thermal analysis, X-ray scattering, and spectroscopy, to provide a comprehensive picture of polymer crystallization.

The author acknowledges the assistance of D. Ho (National Institute of Standards and Technology) with the small-angle neutron scattering experiments and stimulating discussions with F. K. Khoury (National Institute of Standards and Technology), B. Hammouda (National Institute of Standards and Technology), and S. Z. D. Cheng (University of Akron). The author also acknowledges the NSF Career Award, Petroleum Research Fund of the American Chemical Society, the faculty startup fund from Michigan Technological University, and the support of the National Institute of Standards and Technology in providing the neutron research facilities used in this work.

REFERENCES AND NOTES

1. Wunderlich, B. Macromolecular Physics; Academic: New York, 1973.
2. Lauritzen, J. I.; Hoffman, J. D. J Res Natl Bur Stand Sect A 1960, 64, 73.
3. Hoffman, J. D.; Davis, G. T.; Laurizten, J. I. In Treatise on Solid State Chemistry; Hannay, N. B., Ed.; Plenum: New York, 1976; Vol. 3.

4. Khoury, F. A.; Passaglia, E. In Treatise on Solid State Chemistry; Hannay, N. B., Ed.; Plenum: New York, 1976; Vol. 3.
5. Keller, A. Rep Prog Phys 1968, 31, 623.
6. Geil, P. H. Polymer Single Crystals; Interscience: New York, 1963.
7. Hoffman, J. D.; Weeks, J. J Res Natl Bur Stand Sect A 1962, 66, 13.
8. Alamo, R. G.; Viers, B. D.; Mandelkern, L. Macromolecules 1995, 28, 3205.
9. Marand, H.; Xu, J.; Srinivas, S. Macromolecules 1998, 31, 8219.
10. Al-Hussein, M.; Strobl, G. Macromolecules 2002, 35, 1672.
11. Keller, A.; Cheng, S. Z. D. Polymer 1998, 39, 4461.
12. Cheng, S. Z. D.; Keller, A. Annu Rev Mater Sci 1998, 28, 533.
13. Cheng, S. Z. D.; Lotz, B. Philos Trans R Soc London A 2003, 361, 517.
14. Terrill, N. J.; Fairclough, P. A.; Towns-Andrews, E.; Komanschek, B. U.; Young, R. J.; Ryan, A. J. Polymer 1998, 39, 2381.
15. Olmsted, P. D.; Poon, W. C. K.; McLeish, T. C. B.; Terrill, N. J.; Ryan, A. J. Phys Rev Lett 1998, 81, 373.
16. Akpalu, Y. A.; Amis, E. J. J Chem Phys 1999, 111, 8686.
17. Wang, Z. G.; Hsiao, B. S.; Sirota, E. B.; Agarwal, P.; Srinivas, S. Macromolecules 2000, 33, 978.
18. Strobl, G. Eur Phys J E 2000, 3, 165.
19. Lotz, B. Eur Phys J E 2000, 3, 185.
20. Cheng, S. Z. D.; Li, C. Y.; Zhu, L. Eur Phys J E 2000, 3, 195.
21. Muthukumar, M. Eur Phys J E 2000, 3, 199.
22. Jackson, J. F.; Mandelkern, L. Macromolecules 1968, 1, 546.
23. Huseby, T. W.; Bair, H. E. J Appl Phys 1968, 39, 4969.
24. Leung, W. M.; Manley, R. S. J.; Panaras, A. R. Macromolecules 1985, 18, 746.
25. Flory, P. J. J Chem Phys 1947, 15, 684.
26. Flory, P. J.; Vrij, J. Am Chem Soc 1963, 85, 3548.
27. Pennings, A. J. Characterization of Macromolecular Structure; Publication 1573, National Academy of Sciences: Washington, DC, 1968; p 214.
28. Sanchez, I. C.; DiMarzio, E. A. Macromolecules 1971, 4, 677.
29. Hocquet, S.; Dosière, M.; Tanzawa, Y.; Koch, M. H. Macromolecules 2002, 35, 5025.
30. Passaglia, E.; Khoury, F. Polymer 1984, 25, 631.
31. Leung, W. M.; Manley, R. S. J.; Panaras, A. R. Macromolecules 1985, 18, 760.
32. Chen, C. M.; Higgs, P. G. J Chem Phys 1998, 108, 4305.
33. Liu, C.; Muthukumar, M. J Chem Phys 1998, 109, 2536.
34. Dukovski, I.; Muthukumar, M. J Chem Phys 2003, 118, 6648.
35. Hu, W. B. J Chem Phys 2001, 115, 4395.
36. Ruland, W.; Colloid Polym Sci 1977, 255, 417.
37. Strobl, G. R.; Schneider, M. J. J Polym Sci Polym Phys Ed 1980, 18, 1343.
38. Richter, D.; Schneiders, D.; Monkenbusch, M.; Willner, L.; Fetters, L. J. Huang, J. S.; Lin, M.; Mortensen, K.; Farago, B. Macromolecules 1997, 30, 1053.
39. Schelten, J.; Wignall, G. D.; Ballard, D. G. H.; Longman, G. W. Polymer 1977, 18, 1111.
40. Keller, A. Faraday Discuss Chem Soc 1979, 68, 145.
41. Guttman, C. M.; DiMarzio, A.; Hoffman, J. D. Polymer 1981, 22, 597.
42. Guenet, J. M.; Picot, C. Polymer 1979, 20, 1483.
43. Beaucage, G.; Stein, R. S. Macromolecules 1993, 26, 1617.
44. Wang, H.; Nieh, M. P.; Hobbie, E. K.; Glinka, C. J.; Katsaras, J. Phys Rev E 2003, 67, 060902.
45. Imai, M.; Nakaya, K.; Kato, T. Phys Rev E 1999, 60, 734.
46. Imai, M.; Kato, T.; Schneider, D. J Chem Phys 1998, 108, 1710.
47. Angelico, R.; Olsson, U.; Mortensen, K.; Ambrosone, L.; Palazzo, G.; Ceglie, A. J Phys Chem B 2002, 106, 2426.
48. Brennan, T.; Roser, S. J.; Mann, S.; Edler, K. J Chem Mater 2002, 14, 4292.
49. Oda, R.; Weber, V.; Lindner, P.; Pine, D. J.; Mendes, E.; Schosseler, F. Langmuir 2000, 16, 4859.
50. Egelhaaf, S.; Olsson, U.; Schurtenberger, P.; Morris, J.; Wennerstrom, H. Phys Rev E 1999, 60, 5681.
51. Egelhaaf, S. U.; Olsson, U.; Schurtenberger, P. Phys B 2000, 276, 326.
52. Egelhaaf, S. U.; Schurtenberger, P. Phys B 1997, 234, 276.
53. Rossle, M.; Manakova, E.; Holzinger, J.; Vanatalu, K.; May, R. P.; Heumann, H. Phys B 2000, 276, 532.
54. Motoya, K.; Hioki, K.; Suzuki, J. Appl Phys A 2002, 74, S592.
55. Mason, T. G.; Lin, M. Y. J Chem Phys 2003, 119, 565.
56. Gilbert, E. P.; Reynolds, P. A.; Thiyagarajan, P.; Wozniak, D. G.; White, J. W. Phys Chem Chem Phys 1999, 1, 2715.
57. Schwahn, D.; Balz, M.; Bartz, M.; Fomenko, A.; Tremel, W. J Appl Crystallogr 2003, 36, 583.
58. Schwahn, D.; Janssen, S.; Springer, T. J Chem Phys 1992, 97, 8775.
59. Jinnai, H.; Hasegawa, H.; Hashimoto, T.; Han, C. C. J Chem Phys 1993, 99, 4845.
60. Jinnai, H.; Hasegawa, H.; Hashimoto, T.; Han, C. C. J Chem Phys 1993, 99, 8154.
61. Hobbie, E. K.; Merkle, G.; Bauer, B. J.; Han, C. C. Phys Rev E 1995, 52, 3256.

62. Hobbie, E. K.; Merkle, G.; Bauer, B. J.; Han, C. C. Mod Phys Lett B 1996, 10, 1219.
63. Lefebvre, A. A.; Lee, J. H.; Balsara, N. P.; Hammouda, B. J Chem Phys 2002, 116, 4477.
64. Lefebvre, A. A.; Lee, J. H.; Jeon, H. S.; Balsara, N. P.; Hammouda, B. J Chem Phys 1999, 111, 6082.
65. Takenaka, M.; Takeno, H.; Hasegawa, H.; Saito, S.; Hashimoto, T.; Nagao, M. Phys Rev E 2002, 65, 021806.
66. Takenaka, M.; Takeno, H.; Hashimoto, T.; Nagao, M. J Appl Crystallogr 2003, 36, 642.
67. Coutry, S.; Spells, S. J. Polymer 2003, 44, 1949.
68. Willner, L.; Poppe, A.; Allgaier, J.; Monkenbusch, M.; Richter, D. Europhys Lett 2001, 55, 667.
69. Endo, H.; Colfen, H.; Schwahn, D. J Appl Crystallogr 2003, 36, 568.
70. Plestil, J.; Pospisil, H.; Kuklin, A. I.; Cubitt, R. Appl Phys A 2002, 74, S405.
71. Beaucage, G.; Schaefer, D. W. J Non-Cryst Solids 1994, 172, 797.
72. Flory, P. J. Principles of Polymer Chemistry; Cornell University Press: Ithaca and London, 1953.
73. Roe, R. J. Methods of X-Ray and Neutron Scattering in Polymer Science; Oxford University Press: New York, 2000.